Heralded preparation of spin qubits in droplet-etched GaAs quantum dots using quasiresonant excitation

Caspar Hopfmann ⬤,[1,*] Nand Lal Sharma,[1] Weijie Nie,[1] Robert Keil,[1,†] Fei Ding,[2] and Oliver G. Schmidt[1,3,4]

[1]*Institute for Integrative Nanosciences, IFW Dresden, Helmholtzstraße 20, 01069 Dresden, Germany*
[2]*Institut für Festkörperphysik, Leibniz Universität Hannover, Appelstraße 2, 30167 Hannover, Germany*
[3]*Material Systems for Nanoelectronics, Technische Universität Chemnitz, 09107 Chemnitz, Germany*
[4]*Nanophysics, Faculty of Physics and Würzburg-Dresden Cluster of Excellence ct.qmat, TU Dresden, 01062 Dresden, Germany*

We present a comprehensive study on heralded spin preparation employing excited state resonances of droplet-etched GaAs quantum dots. This achievement will facilitate future investigations of spin qubit based quantum memories using the GaAs quantum dot material platform. By observation of excitation spectra for a range of fundamental excitonic transitions, the properties of different quantum dot energy levels, i.e., shells, are revealed. The innovative use of polarization-resolved excitation and detection in the context of quasiresonant excitation spectroscopy of quantum dots greatly simplifies the determination of the spin preparation fidelities—irrespective of the relative orientations of laboratory and quantum dot polarization eigenbases. By employing this method, spin preparation fidelities of quantum dot ground states of up to 85% are found. Additionally, the characteristic nonradiative decay time is investigated as a function of ground state, excitation resonance, and excitation power level, yielding decay times as low as 29 ps for *s-p* shell exited state transitions. Finally, by time-resolved correlation spectroscopy it is demonstrated that the employed excitation scheme has a significant impact on the electronic environment of quantum dot transitions and their apparent brightness.

I. INTRODUCTION

Optically accessible quantum memories are fundamental for implementations of quantum networks as they facilitate the synchronization required for schemes of long-distance quantum information exchange [1–4]. While tremendous progress towards optical quantum networks using entangled photon sources has been achieved in the past decade [5–11], quantum systems that address all of the required aspects—namely high source efficiency, repetition rates, and spin qubit coherence—are still sorely lacking [4]. Atomic and diamond defect based systems feature long quantum storage times required for memory applications, their repetition rate and internal quantum efficiency, respectively, are however fundamentally limited [12,13]. Due to their rapid technological advance, semiconductor quantum dots (QDs) have also received significant attention [7,9,10,14–18]. The main drawback of these systems so far has been that the quantum coherence of their spin qubits is limited by interaction with the nuclear magnetic environment of its constituting atoms, i.e., the Overhauser field [18–20]. While nuclear polarization and spin echo techniques may extend the coherence time of spin qubits significantly [21–23], the achievable values in commonly employed InGaAs/InAs QDs are still limited by the presence of high spin $(+9/2)$ ^{115}In and ^{113}In isotopes. Due to their unique

properties, such as low inhomogeneous broadening, small fine-structure splitting, and compatibility to Rb-based atomic quantum memories [24,25], droplet-etched GaAs QDs established themselves as potent sources of entangled photon pairs [9,10,17,26]. Contrary to the better studied InGaAs/InAs material systems, the absence of high-spin In isotopes in GaAs QDs makes them attractive candidates for extended spin qubit coherence needed for realizing quantum dot spin qubit based quantum memories. A first important step towards realizing these devices is achieved in the presented study, in which it is shown that quasiresonant excitation schemes can be used to initialize fundamental QD spin qubits deterministically. To this end, polarization-resolved excitation spectroscopy and time-resolved pump-probe investigations are combined to obtain a comprehensive picture of the properties of excited states in GaAs quantum dots and their possible applications. This foundational study therefore provides an ideal stepping stone towards future investigations of quantum memories using GaAs QD spin qubits.

Quasiresonant excitation is defined as any driving of discrete excitonic excited states of QDs below the band gap of the surrounding AlGaAs matrix material. These excited states decay down to QD excitonic ground states by nonradiative decay processes such as phonon or Auger electron emission. This driving scheme is distinct from resonant excitation, in which the QD excitonic ground states are driven directly and no nonradiative decay takes place. A comparative analysis of above-band, quasiresonant, and resonant excitation schemes can be found in the Supplemental Material [27]. By observing Rabi oscillations, it has been demonstrated that resonant

---

*c.hopfmann@ifw-dresden.de
†Present address: Fraunhofer-Institut für Angewandte Festkörperphysik (IAF), Tullastraße 72, 79108 Freiburg, Germany.

excitation of basic excitonic transitions in QDs is generally a coherent process [28–30]. Since in quasiresonant excitation a nonradiative decay process is used to drive the basic excitonic two-level systems of QDs, it is more accurately described by a three-level system. Due to the generalized optical Bloch equations, the observability of Rabi oscillations using the quasiresonant driving scheme is therefore dependent on the dephasing introduced by the nonradiative decay processes in contrast to that of the ground state [31]. Rabi oscillations in quasiresonantly excited QDs can only be observed if the parameters of the three-level system of excitation resonance, excitonic ground state, and initial state (cf. Sec. II C) are such that it effectively converges to a two-level system. The required parameter relations are dependent on whether the nonradiative decay process preserves the coherence of the excitation pulse. If it does not, Rabi oscillations can only be observed in case the temporal excitation pulse width T_P is small compared to the dephasing induced by the characteristic nonradiative decay time T_{NR}, i.e., $T_P \ll T_{NR}$. Assuming the nonradiative decay (fully) preserves the excitation coherence, the condition changes to $T_{NR} \ll T_1$, where T_1 is the QD excitonic state lifetime. For InGaAs QDs Rabi oscillations using polarization-resolved quasiresonant excitation have been demonstrated [16]. This has proven essential for the realization of cluster states [7] and spin coherence measurements [18] using these QDs. Answering the question whether similar schemes are also feasible using droplet-etched GaAs QDs is therefore a primary goal of this study.

The rigorous demonstration of deterministic preparation of QD spin qubits requires proper initialization of the spin qubit ground state. As this initialization is not performed in this study, deterministic spin preparation is only achieved for the neutral exciton. This is because of its vacuum ground state, for which no preparation is needed [16,32]. The preparation of a single carrier spin qubit, i.e., a single electron or heavy hole in the QD ground state, on the other hand is heralded by the emission of a photon from the respective trionic transition, due to the presence of spin-photon entanglement [15,33]. The fidelity of the spin qubit preparation for neutral exciton and charged states alike can therefore be characterized by correlating the degrees of polarization of the QD excitation and emission. Evaluating this fidelity for droplet-etched GaAs QDs is another principle objective of this study.

II. RESULTS AND DISCUSSION

A typical above-band photoluminescence (PL) spectrum of a single QD is shown if Fig. 1(a) in saturation of the neutral QD exciton X_S^0 transition. Though the general shape of GaAs quantum dot spectra has been established previously [34], the exact energy differences between the emission lines depend on the Al concentration of the QD matrix material. Contrary to In(Ga)As-based quantum dots, which are grown using the Stranski-Krastanov process, the spectral properties—such as the energetic distribution of fundamental emission lines—of droplet-etched GaAs quantum are much more consistent [25]. In Fig. 1(b) transitions of four basic excitonic QD charge configurations, namely X_S^0, X_S^+, and $X_S^- + XX_S^0$, are indicated. X_S^+ and X_S^- represent the positively and negatively charged trions, respectively, and XX_S^0 the neutral biexciton. The transitions
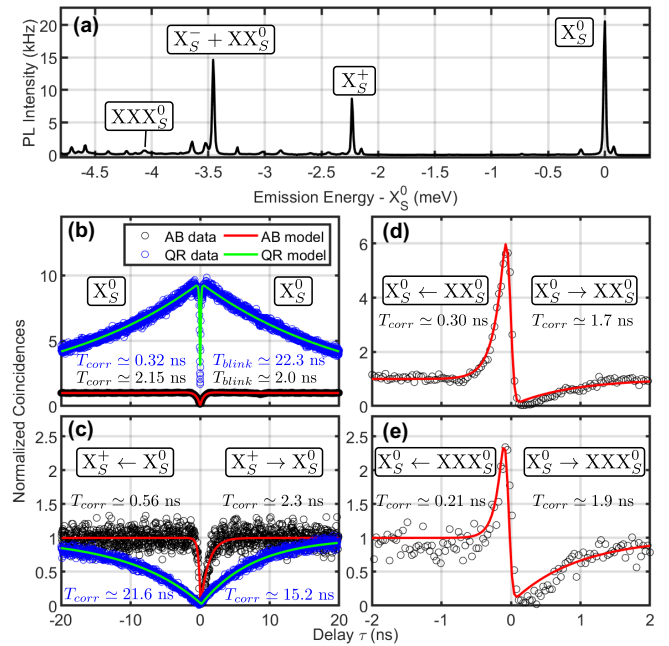
FIG. 1. (a) Typical spectrum of a single GaAs QD using above-band excitation. Selected fundamental emission lines (cf. Table I) are annotated. (b) and (c)–(e) X_S^0 two-photon auto- and cross-correlation traces, respectively, as a function of the time delay τ between detection events. Recorded (modeled) correlation curves using above-band (AB) and quasiresonant (QR, $\Delta_{ex} = 10.08$ meV, cf. Fig. 2) excitation are drawn in black (red) and blue (green), respectively. The full QR data set is shown in Fig. S4 [27]. Cross correlations (c)–(e) are recorded between X_S^0 and X_S^+, $X_S^- + XX_S^0$, as well as XXX_S^0, respectively. Modeling of the correlation traces is performed using Eqs. (1)–(4) and the extracted parameter values are summarized in Table II. The characteristic correlation timescales T_{corr} are annotated in the graphs.

were identified using a combination of polarization, power dependent PL, and PL excitation (PLE) spectroscopy, details are given in the following sections and in the Supplemental Material [27]. Due to the spectral resolution limit of 15 eV, the $X_S^- + XX_S^0$ transition lines cannot be separated in PL spectroscopy. As detailed in Sec. II B, both transitions however feature distinct excitation resonances and can therefore be pumped selectively. Using this property and comparison of the central emission energies, which can be determined to an accuracy of about 0.5 μeV (cf. Supplemental Material Fig. S1 [27]), it is possible to estimate the energetic splitting of X_S^0 and XX_S^0 transitions to 5 μeV [35]. Spectral overlap between the X_S^- and XX_S^0 transitions is observed consistently for matrix material Al concentrations of 15%. The nomenclature of fundamental QD transitions used throughout this work is summarized in Table I.

A. Correlation spectroscopy

Figures 1(b)–1(e) depict two-photon auto- and cross-correlation traces $g(\tau)$ using continuous wave (cw) excitation of selected combinations of emission lines. The curves are

TABLE I. Description of various optical transitions of GaAs QDs embedded in $Al_{0.15}Ga_{0.85}As$ matrix material using the nomenclature established by Benny et al. [36]. ke^l (kh^l) represents electron (hole) occupation l of the kth excitation level, i.e., $k = 1$ s shell and $k = 2$ p shell. The subscript of the QD transition labels refers to the shell in which the observed electron-hole recombination takes place. Relative emission energies with respect to X_S^0 ($E_{X_S^0} = 1.5880$ eV) are determined by polarization and power dependent high resolution spectroscopy, cf. Figs. 1(a) and S1 [27].

Label	Transition	$\Delta_{i-X_S^0}$ (meV)
X_S^0	$(1e^1)(1h^1) \to 0$	0
X_S^+	$(1e^1)(1h^2) \to (1h^1)$	-2.24
XX_S^0	$(1e^2)(1h^2) \to (1e^1)(1h^1)$	-3.47
X_S^-	$(1e^2)(1h^1) \to (1e^1)$	-3.48
XXX_S^0	$(1e^22e^1)(1h^22h^1) \to (1e^12e^1)(1h^12h^1)$	-4.09

modeled, depending on the nature of the correlation between two QD transitions i and j, according to

$$g^{(2)}(\tau) = [g_{ij}(\tau)g_{blink}(\tau)]\mathcal{N}_{Det}(\delta_{2det}) + 1, \quad (1)$$

$$g_{ij}^{(2)}(\tau) = (g_0 - 1)e^{-\frac{|\tau|}{T_{corr}}}, \quad (2)$$

$$g_{blink}^{(2)}(\tau) = \left(\frac{1}{\beta} - 1\right)e^{-\frac{|\tau|}{T_{blink}}}. \quad (3)$$

$g^{(2)}$ is the autocorrelation function of second order, T_{corr} and T_{blink} are the characteristic correlation and blinking timescales, respectively, β is the blinking on-off ratio, and τ is the time delay between two photon detection events. The (anti-)bunching $g_{ij}^{(2)}(\tau \to 0)$ is represented by $g_0 \geqslant 1$ ($0 \leqslant g_0 < 1$). $g_{blink}^{(2)}(\tau)$ models spectral blinking of the investigated line in autocorrelation experiments and is adopted from Jahn et al. [24]. β is a function of the height of the autocorrelation bunching, while T_{blink} is related to its decay towards increasing delay times. Experimentally the correlation traces are obtained by spectrally filtered two-photon correlation spectroscopy. The width of the spectral window is about 25 μeV. As a consequence, a transition is considered as blocked either if the quantum dot charge state changes or the transition undergoes spectral dephasing out of the spectral window in between two photon detection events. In the limit of an adiabatic excitation scheme, i.e., without influence of

saturation effects, T_{corr} is equivalent to the radiative lifetime T_1, i.e., $T_{corr} \to T_1$. In order to take into account the limited temporal response of the detection system, the raw autocorrelation trace is convoluted with the bidetector response function $\mathcal{N}_{Det}(\delta_{2det})$, modeled by a normal distribution of FWHM $\delta_{2det} = 75$ ps. Equation (1) can be adopted for cross correlations by differentiating between regimes $\tau_{i \to j} > 0$ and $\tau_{i \leftarrow j} > 0$, effectively yielding two correlation timescales that represent switching between emission events of two different QD transitions i and j:

$$g_{cross}^{(2)}(\tau) = [\Theta(\tau) g_{i \to j}(\tau) + \Theta(-\tau) g_{i \leftarrow j}(\tau)]\mathcal{N}_{Det}(\delta_{2det}) + 1. \quad (4)$$

Θ is the Heaviside step function while $g_{i \to j}$ and $g_{i \leftarrow j}$ are given by Eq. (2). The parameter values obtained by modeling of the correlation traces are summarized in Table II.

Both X_S^0 autocorrelation traces of Fig. 1(b) exhibit strong antibunching and are modeled according to Eq. (1). The estimated parameter values related to the blinking are $\beta^{632\,nm} = 0.86 \pm 0.01$ and $T_{blink}^{632\,nm} = (2.0 \pm 0.1)$ ns, for quasiresonant excitation values of $\beta^{QR} = 0.06 \pm 0.01$ and $T_{blink}^{QR} = (22.3 \pm 0.3)$ ns are obtained. While the $g^{(2)}(0)$ values for both excitation schemes are comparable, the modeled correlation timescales are divergent. This is discussed in more detail below. Blinking of the X_S^0 emission line is much more pronounced in quasiresonant compared to above-band excitation, as can be observed in the autocorrelation trace by the strong bunching and its decay, similarly observed elsewhere [24]. We attribute this behavior to two effects: First, the fluctuating population of defect states in the matrix material environment of the QD influence its energetic structure through the Stark effect thereby causing spectral jitter of the QD transitions [37–39]. These defect states may get saturated in the case of above-band excitation, but not in resonant pumping [40]. Second, the average QD charge state may get reconfigured depending on the employed excitation scheme [41]. We observe that the average QD charge becomes generally more positive in quasiresonant excitation.

In Fig. 1(c) traces of cross correlations between X_S^+ and X_S^0 are depicted for both above-band and quasiresonant excitation schemes. The two correlation traces provide information with respect to the charge fluctuations between neutral and positively charged states of the QD. Again, as in the case of the X_S^0 autocorrelation, the charge related blinking behavior is

TABLE II. Estimated parameter values according to Eqs. (1) to (4) of the auto- and cross-correlation traces shown in Figs. 1(b)–1(e), respectively. The abbreviations AB and QR stand for above-band and quasiresonant excitation schemes, respectively. Errors are statistically estimated by 1σ confidence intervals.

Fig. 1	Transition i	j	$g^{(2)}(0)$ $i \to j$	$j \to i$	T_{corr} (ns) $i \to j$	$j \to i$
b(AB)	X_S^0		0.023 ± 0.006		2.15 ± 0.07	
b(QR)	X_S^0		$0.00 + 0.02$		0.32 ± 0.01	
c(AB)	X_S^0	X_S^+	$0.00 + 0.03$		0.56 ± 0.07	2.3 ± 0.1
c(QR)	X_S^0	X_S^+	0.025 ± 0.004		21.6 ± 0.3	15.2 ± 0.3
d(AB)	X_S^0	XX_S^0	$0.00 + 0.04$	9.4 ± 0.1	0.303 ± 0.006	1.70 ± 0.09
e(AB)	X_S^0	XXX_S^0	$0.00 + 0.04$	3.8 ± 0.3	0.21 ± 0.03	1.9 ± 0.2
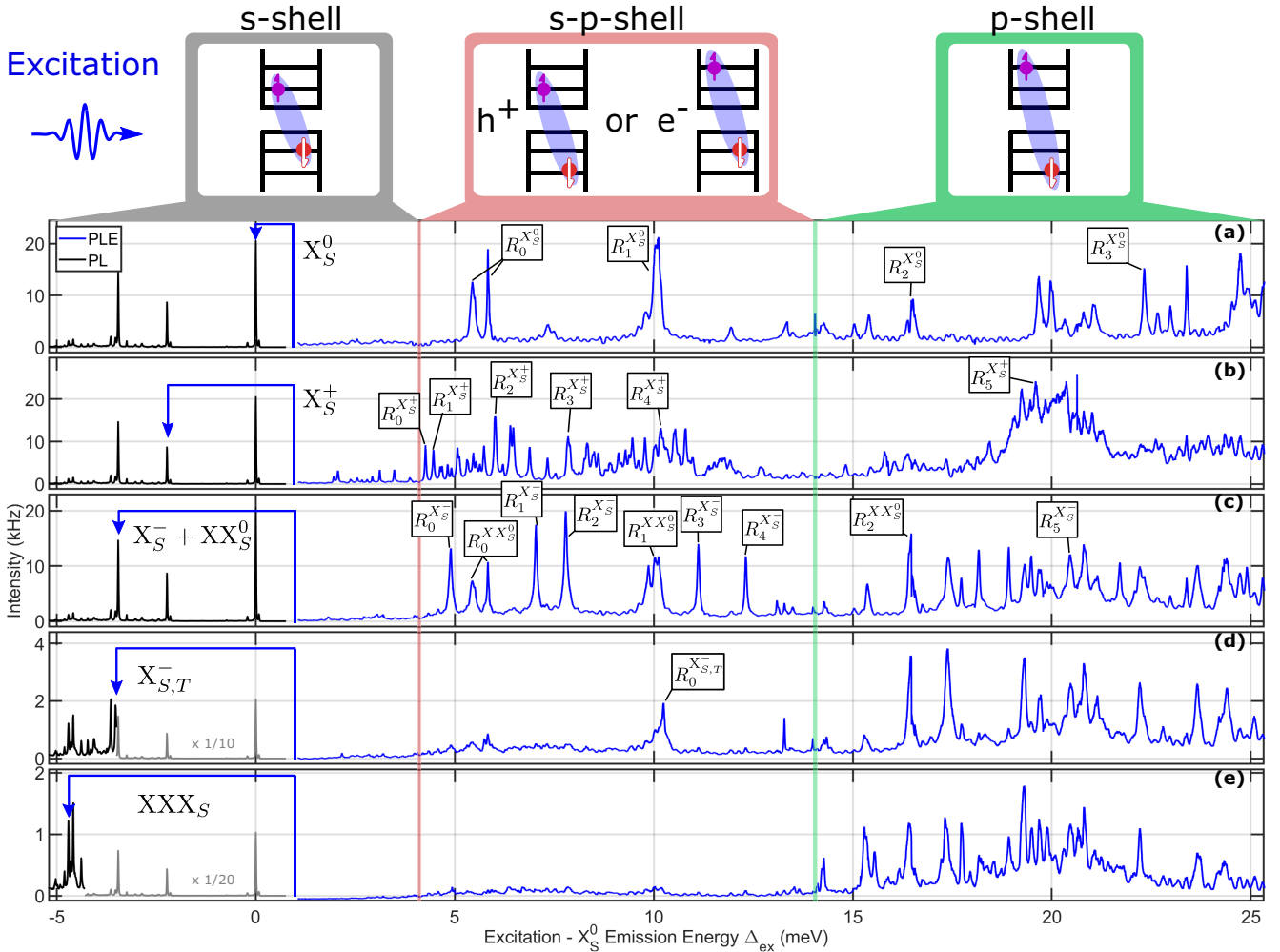
FIG. 2. Combined PLE (blue) and PL (black) spectra of selected *s*-shell transitions (cf. Table I) obtained by integration over *s*-shell emission lines as a function of the relative energy between excitation laser and X_S^0 emission energy Δ_{ex}. Different resonances and excitation shells are annotated, for details see Table III and text. Above-band spectra are recorded at X_S^0 saturation excitation power of 1.5 μW, while the PLE spectra are recorded by employing 1.2 μW quasiresonant laser excitation.

very different in the two excitation schemes. In above-band pumping the fluctuations take place on shorter timescales compared to quasiresonant excitation. The reason for this is that in the latter there are far fewer free carriers in the matrix material surrounding the QD—which in turn enhances the stability of the QD charge state. Under the assumption that both X_S^0 and X_S^+ are pumped equivalently—which is a valid assumption for above-band excitation—the intensity ratio between X_S^0 and X_S^+ lines can independently be determined from the ratio $T_{corr}^{632\,nm}(X_S^0 \rightarrow X_S^+)/T_{corr}^{632\,nm}(X_S^+ \rightarrow X_S^0) \simeq 4.3$. This value qualitatively matches the intensity ratio determined from the PL spectrum of Fig. 1(a) of 2.8. Due to the presence of a double X_S^0 and X_S^+ resonance at $\Delta_{E_i-E_{X_S^0}} = 10.8$ meV, cf. Fig. 2, the assumption of equivalent excitation conditions for both lines can be extended also to the quasiresonant excitation scheme in this particular case. The resulting intensity ratio $T_{corr}^{QR}(X_S^0 \rightarrow X_S^+)/T_{corr}^{QR}(X_S^+ \rightarrow X_S^0)$ is about 0.7 which demonstrates that the QR excitation scheme favors positive charge states in the QD. This result is a consistent observation for

GaAs quantum dots, but the exact mechanism of this effect remains unclear and is beyond the scope of this work.

In Fig. 1(d) the cross correlation between the X_S^0 and $X_S^- + XX_S^0$ emission lines is shown. As expected from the $XX_S^0 \rightarrow X_S^0$ cascade a strong bunching is observed, while the $X_S^0 \rightarrow XX_S^0$ process is antibunched [42]. Due to the nature of the cascade, for each emission of a XX_S^0 photon, the X_S^0 state is inherently adiabatically prepared. Therefore, $T_{corr}(XX_S^0 \rightarrow X_S^0)$ is equivalent to the X_S^0 lifetime $T_1^{X_S^0} = (0.303 \pm 0.006)$ ns, which matches the value $T_{corr}^{QR} = (0.32 \pm 0.01)$ ns recorded at saturation power $P_{sat} = 8$ μW. As a consequence, we conclude that the quasiresonant excitation is adiabatic (i.e., $T_{corr}^{QR} \rightarrow T_1$), at least in the case of the specific resonance used. The latter is further discussed using results of the PLE and pump-probe experiments. This finding is in stark contrast to the timescale of $T_{corr}^{632\,nm} = (2.15 \pm 0.07)$ observed in the autocorrelation trace of Fig. 1(b). For the employed excitation power of 1.5 μW $\simeq P_{sat}$ above-band excitation is therefore clearly not adiabatic.

TABLE III. List of annotated excitation resonances of Figs. 2(a)–2(c). Excitation resonance energies Δ_{ex} are given relative to the s-shell X_S^0 transition. The accuracy of Δ_{ex} is estimated to 6.5 μeV. Each excitation resonance is attributed to a specific series of transitions, called shells. Details and definitions are found in the text. Excitation saturation powers P_{sat} and nonradiative decay times T_{NR} obtained by modeling of pump-probe experiments, cf. Figs. 3 and S3 [27], are shown for selected resonances. The statistical standard deviation of T_{NR} is about 1% at P_{sat} and to about 5% at 0.04 P_{sat}. The spectral widths associated with the excitation resonances are discussed in the Supplemental Material [27].

s shell	Ex. Res.	Δ_{ex} (meV)	Shell	P_{sat} (μW)	T_{NR} (ps)
	$R_0^{X_S^0}$	5.444	s-$p(h^+)$	13	163.0
		5.830			
X_S^0	$R_1^{X_S^0}$	10.100	s-$p(e^-)$	8	218
				0.04 P_{sat}	36.9
	$R_2^{X_S^0}$	16.472	p	14	389
	$R_3^{X_S^0}$	22.324	p	6	385
	$R_0^{X_S^+}$	4.264	s-$p(h^+)$		
	$R_1^{X_S^+}$	4.464	s-$p(h^+)$		
	$R_2^{X_S^+}$	6.017	s-$p(h^+)$	6	129
				0.03 P_{sat}	88.3
X_S^+	$R_3^{X_S^+}$	7.781	s-$p(h^+)$		
	$R_4^{X_S^+}$	10.179	s-$p(e^-)$	9	210
	$R_5^{X_S^+}$	19.591	p	1	165
	$R_0^{X_S^-}$	4.900	s-$p(h^+)$	10	56.8
				0.04 P_{sat}	29.1
	$R_1^{X_S^-}$	7.040	s-$p(h^+)$		
X_S^-	$R_2^{X_S^-}$	7.786	s-$p(h^+)$	20	74.1
	$R_3^{X_S^-}$	11.119	s-$p(h^+)$		
	$R_4^{X_S^-}$	12.305	s-$p(h^+)$		
	$R_5^{X_S^-}$	20.464	p	4	240
	$R_0^{XX_S^0}$	5.444	s-$p(h^+)$		
		5.834			
XX_S^0	$R_1^{XX_S^0}$	10.027	s-$p(e^-)$		
	$R_2^{XX_S^0}$	16.469	p		

Figure 1(e) depicts a cross-correlation trace between XXX_S^0 and X_S^0 emission lines recorded using above-band excitation. Analogous to the correlation trace of Fig. 1(d), a clear cascade behavior—although with a lower bunching—is observed. We therefore attribute the emission line to a triexciton s-shell emission line, cf. Table I. As detailed in the following section, identification of XXX_S^0 facilitates the inference of the lower energetic bound of p-shell excitation resonances.

B. Excitation spectroscopy

Excited state resonances are characterized by cw PLE spectroscopy employing excitation energies relative to the X_S^0 transition Δ_{ex} in the range of 1 to 25 meV. The resulting PLE spectra (blue lines) of several s-shell QD emission lines are depicted in Fig. 2 as a function of Δ_{ex}. Reference s-shell emission spectra (black lines) obtained using above-band ex-

citation are shown for comparison. The s-shell transitions, which are numerically integrated as a function of Δ_{ex} in order to obtain the PLE spectra, are indicated by blue arrows. The spectral integration window is equivalent to the observed full-width half-maximum (FWHM) of the s-shell transitions. The resolution of the PLE spectra is better than 6.5 μeV, limited only by the accuracy of the employed tunable laser system of 2 pm and the step size used to measure the spectra. The excitation laser step size is kept below 5 μeV for all PLE investigations. As can readily be seen from the PLE spectra, a significant number of resonances can be found in the presented Δ_{ex} range. Resonances that are relevant for further discussion are annotated in the figure and detailed in Table III. For InGaAs QDs grown in the Stranski-Krastanov mode unambiguous identification of many excited state resonances has been demonstrated [36,41,43–45]. Though the same would in principle also be possible for excited states of GaAs QDs used in this study, the energetic structure of these QDs is different as outlined below. Taking into account the fact that there is presently no theory model for the energetic structure of droplet-etched GaAs QDs, the rigorous identification of the PLE resonances to specific QD multicarrier excitations—beyond some general observations—is outside the scope of this work and is left to future studies.

Resonances $R_0^{X_S^0}$ and $R_0^{XX_S^0}$ of PLE spectra in Figs. 2(a) and 2(c), respectively, are equivalent because every biexcitonic photon emission is necessarily followed by emission of X_S^0 due to the neutral exciton cascade, cf. Fig. 1(d). By using this the association between the PLE spectra of $X_S^- + XX_S^0$ it is possible to separate resonances of X_S^- and XX_S^0 which are intermingled in Fig. 2(c). The annotated resonances reflect this association. By comparison with PLE scans performed on InGaAs QDs of Ref. [41] resonances $R_0^{X_S^0}$ and $R_0^{XX_S^0}$ can be identified as the excited state configuration $(1e^1)(2h^1)$. In the study of Benny et al. this excited state was identified at a Δ_{ex} of about 16 meV, which is an increase of about three times compared to the GaAs QDs used in this study. It can therefore be concluded that the energetic splittings in the confinement potential of GaAs quantum dots are significantly lower. We attribute this difference to the fact that droplet-etched GaAs QDs are larger in their dimensions both parallel and perpendicular to the growth direction [34]. Furthermore, compared to the InGaAs QDs of Ref. [41] the energetic splitting of the heavy holes in GaAs QDs is significantly lower, which can be observed in the comparatively smaller energy separation between PLE resonances of Figs. 2(b) and 2(c). For example, The energetic splitting between $R_0^{X_S^+}$ and $R_1^{X_S^+}$ is (0.20 ± 0.02) meV, while for $R_0^{X_S^-}$ and $R_1^{X_S^-}$ it equates to (2.12 ± 0.02) meV, yielding a 10.7-fold reduction of the X_S^+ compared to X_S^- excited state resonance splittings. The exact mechanism causing the dissimilar energetic splittings of electronic sublevels is currently not known, we think it could be influenced significantly by the difference of the confinement potential depths between electrons and holes.

While the exact identification of most excited state resonances is beyond the scope of this study, it is clear that there should be different series of excitation resonances—very much analogous to the spectral series (Lyman, Balmer, Paschen, etc.) in hydrogen atoms [46]—present in this system.

Just as in the case of hydrogen atoms, the excitation resonance with the lowest Δ_{ex} can be considered the fundamental transition, while the series of excitation resonances extends towards increasing Δ_{ex}. In contrast to atoms in QDs, the individual transitions of a series originate not from higher order electronic orbitals but from transitions between different excitonic (spin) complexes. In order to accommodate this difference the series of excitation state resonances in QDs are henceforth called shells. The relevant ones for the discussion of the PLE spectra of Fig. 2 are: s shell $[|0\rangle \rightarrow (1e^1)(1h^1)]$, s-p shell (h^+) $[\rightarrow (1e^1)(2h^1)]$, s-p shell (e^-) $[\rightarrow (2e^1)(1h^1)]$, and p shell $[\rightarrow (2e^1)(2h^1)]$, defined in accordance to [41]. The fundamental transitions of each shell are presented schematically at the top of Fig. 2. Since the PLE trace of Fig. 2 was recorded at about one third of the typical saturation intensity of most transitions of about 4 μW, it can be concluded that the relative intensities of the different excitation resonances generally reflect the strength of the light-matter interaction matrix element of the individual transitions. Due to the nature of the different energetic orbitals of electronic states in QDs, the dipole moment between individual series of excitation resonances can be significantly different [36,45]. At the boundary between s and s-p shell resonances we therefore expect to detect a significant change in the intensity of the observed basic s-shell transitions [Figs. 2(a)–2(c)]. Consequently, we attribute the first bright PLE resonances to the lower boundary of the s-p shell of $\Delta_{ex} \simeq 4.2$ meV. This boundary is indicated in Fig. 2 by a red line.

In Fig. 2(d) the PLE spectrum of a spin-blockaded negative trion $(X_{S,T}^-)$ is shown. This state is a negatively charged exciton in which the electron spin configuration is such that a single electron spin is locked in the p shell by the Fermi exclusion principle due to equivalent spins of s- and p-shell electrons. The details and properties of this state are discussed elsewhere [47]. Due to the presence of an electron in the p shell the s-p-shell (h^+) transitions are blocked, while the ones of the electron, i.e., the s-p shell (e^-), are still allowed. The consequence can be seen in the PLE spectrum: most resonances $\Delta_{ex} < 14$ meV that are observed in Figs. 2(a)–2(c) are absent, which also confirms the identity of the observed s-shell emission line. We therefore conclude that the absent excitation resonances belong to the s-p shell (h^+), while $R_0^{X_{S,T}^-}$ belongs to the s-p shell (e^-).

Figure 2(e) depicts the PLE spectrum of an s-shell line we associate with the s-shell transition of a triexcitonic complex $[(1e^2 2e^1)(1h^2 2h^1)]$. As a consequence both s-p shells are absent in its PLE spectrum. The first excitation resonance can therefore be found in the p shell, which enables the estimation of the lower p-shell boundary to $\Delta_{ex} \simeq 14.1$ meV. This is indicated in Fig. 2 by a green line. Around $\Delta_{ex} \simeq 20$ meV a broad maximum in the PLE spectra, especially in the one of X_S^+, is observed. This can be attributed to the overlap of p-shell transitions of both electrons and holes and not to effects related due to phonon-enhanced absorption—which would be expected beyond $\Delta_{ex} \gtrsim 32$ meV [41,48].

C. Pump-probe correlation spectroscopy

In order to investigate the nonradiative decay mechanism of the excitation resonances, pump-probe experiments are
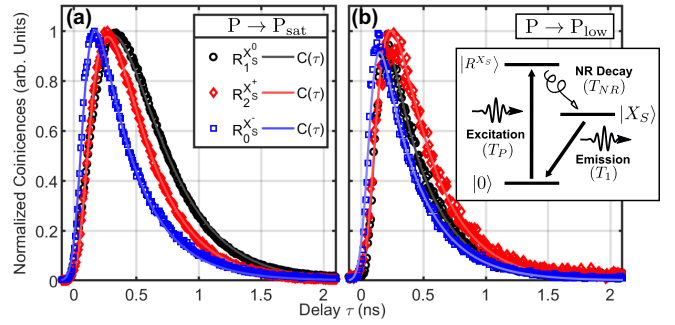
FIG. 3. Quasiresonant pump-probe correlation measurements of fundamental QD transitions X_S^0, X_S^+, and X_S^- at their respective excitation resonances (a) at excitation saturation and (b) far below saturation power P_{sat}. The curves are modeled according to Eq. (5) with T_{NR} as the only free parameter. Specific resonances, excitation conditions, and estimated T_{NR} values are summarized in last two columns of Table III. Inset: Schematic illustration of the three-level system between initial state $|0\rangle$, excitonic s-shell state $|X_S\rangle$, and excited state resonance $|R^{X_S}\rangle$ in the context of quasiresonant pump-probe investigations. The relevant timescales of the pump T_P, the nonradiative decay (NR) to the s-shell T_{NR}, and optical decay of X_S are indicated in brackets.

conducted. The goal of these investigators is to find out on which timescale the nonradiative decay takes place for different excitation resonances and if it is consistent with the assumption of a single or multistage decay process. In these investigations specific excitation resonances are pumped by a pulsed laser while the time-resolved emission of the respective s-shell transition is monitored. The investigated system can therefore be described by a three-level system between initial state $|0\rangle$, excitonic s-shell state $|X_S\rangle$, and excited state resonance $|R^{X_S}\rangle$, cf. Fig. 3. The results for selected X_S^0, X_S^+, and X_S^- transitions and resonances pumped at and far below ($\approx 0.04 P_{sat}$) excitation saturation are shown in Figs. 3(a) and 3(b), respectively. Further results of pump-probe experiments are plotted in Fig. S3 [27]. The intensity correlation data is modeled by a delayed exponential decay function

$$C(\tau) = e^{-\frac{\tau}{T_1^{X_S^0}}} \theta(\tau) \left(\frac{e^{-\frac{\tau}{T_{NR}}}}{T_{NR}} \mathcal{N}_{Det}(\delta_{1det}) \right), \qquad (5)$$

where the nonradiative decay time T_{NR} is the only free parameter. The other parameters, the lifetime $T_1^{X_S^0}$ and the single-photon detection timing jitter δ_{1det}, are fixed to values of 0.303 and 0.053 ns determined externally, cf. Secs. II A and IV, respectively. The delay which is induced by a single particle nonradiative decay process is modeled by an exponential distribution $\frac{e^{-\frac{\tau}{T_{NR}}}}{T_{NR}}$. This simple assumption fits the experimental data very well for most resonances, for the curve shown in Fig. S3(c) [27] the model shows deviations to the experimental data. This can be attributed to the breakdown of the assumption of a single stage decay process. A summary of the extracted T_{NR} values can be found in Table III. It is worth noting that the excitation pulse temporal width $T_P \simeq 3.5$ ps can be safely neglected in this discussion as it is far smaller than T_{NR}, i.e., $C(T_{NR})C(T_P) \approx C(T_{NR})$. For all basic QD charge states the decay time increases towards

elevated values of Δ_{ex} and towards excitation power saturation. As a consequence, the observed excitation resonances with the lowest T_{NR}—and therefore the most direct excitation process—can be found in the s-p shells. Far below saturation, where the influence of the excitation laser induced increase of the decay time should be neglectable, the T_{NR} values of (37 ± 2), (88 ± 2), and (29 ± 1) ps are determined for the QD s-shell transitions X_S^0, X_S^+, and X_S^-, respectively. The excitation resonances in which an additional electron is present in the QD exhibit the fastest nonradiative decay times, while if an additional hole is present, the decay is about a factor of 3 slower. Consequently, the value of T_{NR} in the absence of additional carriers lies between the two former cases. At saturation $T_{NR}^{X_S^0}$, $T_{NR}^{X_S^+}$, and $T_{NR}^{X_S^-}$ values increase to (218 ± 3), (129 ± 2), and (57 ± 1) ps, respectively. Since these values remain below T_1, we conclude that quasiresonant excitation can be used to deterministically prepare GaAs QD ground states in the time domain. Note that no Rabi oscillations, a sign of coherent preparation of the QD s-shell ground states [16,28,29], are observed for any excitation resonance. The reason is that the required observability condition $T_{NR} \ll T_1$ ($T_P \ll T_{NR}$), assuming perseverance (loss) of the excitation coherence by the nonradiative decay mechanisms, is not fulfilled at saturation of the excitation resonances. Judging from the extracted values of T_P, T_{NR}, and T_1 at excitation saturation, for which $T_P \ll T_{NR}$ is better fulfilled than $T_{NR} \ll T_1$, and the observed absence of Rabi oscillations it may seem that there is some evidence that the nonradiative decay mechanism is at least partially preserving the coherence of the excitation pulse. However, since other potential dephasing mechanisms (such as spin-flips) cannot be ruled out, no conclusion on the nature of the nonradiative decay mechanism can be drawn based on this weak indication. Overlap of multiple excitation resonances due to the 100 GHz spectral width of the employed pulsed excitation may be an additional hindrance to the observation of Rabi oscillations. This is the case especially for excitation resonances of the positive charge state, because of the high spectral density of its resonances, cf. Fig. 2(b). The relation between the natural spectral line broadening induced by the lifetime of the excited states and the observed widths of the PLE resonances of Fig. 2 are discussed in more detail in the Supplemental Material [27].

D. Polarization-resolved emission spectroscopy

Due to the quantum mechanical selection rules, spins of excitonic complexes in QDs and the polarization of emitted photons from these transitions are interdependent. A convenient method of characterizing the spin properties of carriers in QDs is therefore to investigate the polarization characteristics of light emitted by their optical transitions [15,33]. For these investigations we employ measurements in six orthogonal polarization bases: H, V, D, A, R, and L that span a Poincaré sphere featuring the principle axes H-V, D-A, and R-L. The degree of polarization along the polarization axes I-J can be determined by $\mathrm{PolDeg(I\text{-}J)} = \frac{\rho(I) - \rho(J)}{\rho(I) + \rho(J)}$, where ρ is the measured spectral intensity associated with the respective polarization base. Note that the degree polarization along the principle axes is equivalent to the normalized Stokes parameters s1, s2, and s3. Further details on the employed
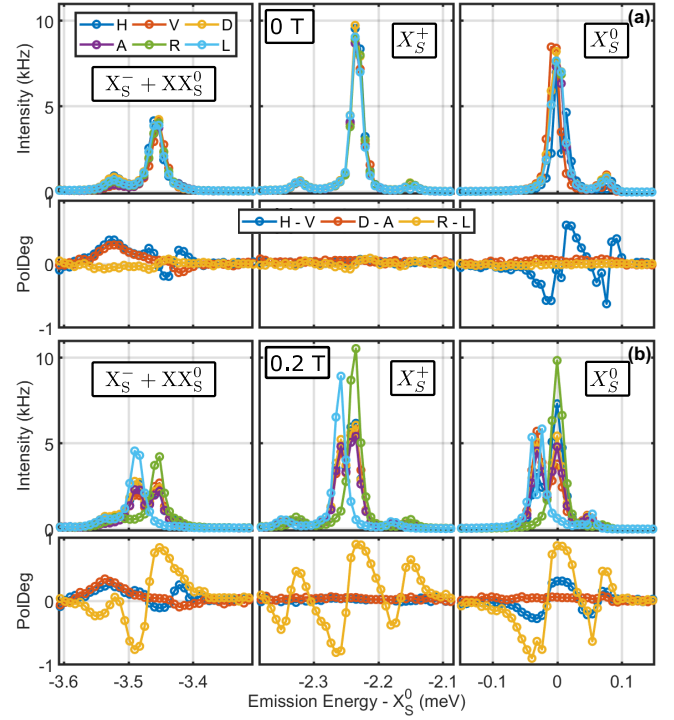
FIG. 4. Polarization-resolved PL spectra of $X_S^- + XX_S^0$, X_S^+, and X_S^0 without applied external magnetic field (a) and with a field of 0.2 T in Faraday configuration (b), respectively. The spectra are recorded using above-band excitation at $P \simeq P_{sat}/2$. The raw spectra are shown in the upper panels, while in the lower ones the degree of polarization (PolDeg, see text) between orthogonal bases are depicted.

polarization definitions can be found in the Supplemental Material [27]. In order to accurately reconstruct the carrier spin states in QDs the QD spin eigenbases need to be calibrated with respect to the laboratory polarization projection. The rotation of the QD and laboratory polarization eigenbases is fully determined by two rotations around the principle polarization axes. In the absence of an external magnetic field, X_S^0 features a fine-structure splitting of 10.1 μeV (cf. supplemental Fig. S1 [27]) due to its integer quasiparticle spin $j_{X_S^0} = \pm 1$. This splitting is oriented along the H-V polarization axis, cf. Fig. 4(a). For finite magnetic fields along the growth direction (Faraday configuration), depending on the field strength, the eigenstates are oriented on a superposition axes of H-V and R-L and are split according to the Zeeman splitting [43], cf. Fig. 4(b). X_S^+ and X_S^- do not exhibit a fine structure in the absence of a magnetic field ($j_{X_S^+} = \pm 1/2$, $j_{X_S^-} = \pm 3/2$) due to the Kramers degeneracy of half-integer spin states [43,49]. Their polarization eigenbase is therefore R-L. Due to the overlap of the $X_S^- + XX_S^0$ transitions, the signature of the XX_S^0 fine-structure splitting in the polarization-resolved spectra is masked. In consequence, the calibration between the QD and laboratory polarization eigenbases is obtained from the H-V splitting of the X_S^0 transition without magnetic field and from the R-L splitting of the X_S^+ transitions in the presence of an external magnetic field as shown in Fig. 4. We employ a small magnetic field of 0.2 T to avoid misalignment of the optical system due to magnetically induced forces. A more detailed
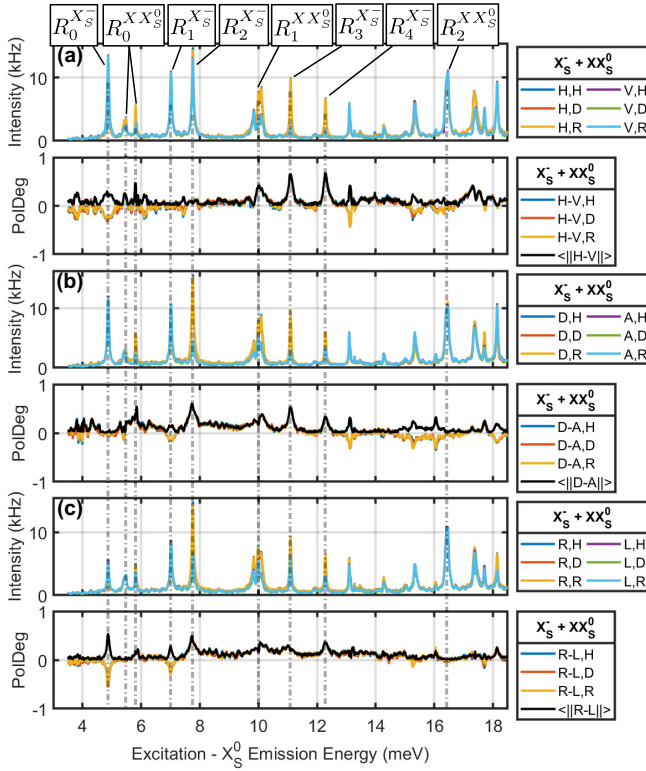
FIG. 5. Exemplary polarization-resolved PLE spectra and polarization degrees (PolDeg) in 18 different combinations of excitation and detection polarization bases (I,J) of the $X_S^- + XX_S^0$ emission lines. The data corresponds to the third run of Fig. 6. The first (I) and second (J) bases are of the excitation and detection, respectively. Upper panels: Combinations with excitation polarization bases (a) H/V, (b) D/A, and (c) R/L. The respective excitation PolDegs are shown in the lower panels. Additionally, total PolDegs of each excitation axes $\langle\|$I-J$\|\rangle$ according to Eq. (6) are drawn. Resonances corresponding to Table III are annotated.

investigation of the Zeeman splitting and diamagnetic shift as well as the fine-structure splitting of droplet-etched QDs can be found in the Supplemental Material [27]. The degree of polarization of Fig. 4 shows that this calibration is not fully equivalent for all investigated transitions. This effect can be attributed to the wavelength dependent birefringent behavior of the employed GaP microlenses (see Methods section)—as this effect is not present in samples without these lenses.

E. Polarization-resolved excitation spectroscopy

Polarization-resolved PLE spectra are depicted exemplarily in Fig. 5 for the $X_S^- + XX_S^0$ transitions. Polarization-resolved PLE spectra of X_S^0 and X_S^+ emission lines are found in Figs. S7 and S8 [27], respectively. As can readily be observed, the behavior of the various resonances is not equivalent, cf. $R_1^{X_S^-}$ vs $R_2^{X_S^-}$ vs $R_3^{X_S^-}$. There are two reasons for this, both of which can be negated similarly to the polarization-resolved PL by calibration of the excitation polarization bases to the spin eigenstates of the specific excitation resonance. First, the polarization calibration of the excitation changes significantly with wavelength due to the birefringent behavior of the GaP

microlens. Second, the excitation resonances originate from different excitonic complexes with distinct spin configurations. Depending on whether the excited and ground state spin symmetries match and if the nonradiative decay process preserves the initial spin created in the excited state, the polarization of the QD excitation and emission are correlated. In order to extract this correlation, which constitutes the s-shell spin preparation fidelity, in the presence of the birefringent GaP microlens the PLE spectra of Fig. 5 are measured in 18 different combinations of polarization bases, i.e., six excitation and three detection bases. To avoid calibrating each excitation resonance separately, the excitation polarization degree $\langle\|$I-J$\|\rangle$ may be defined as

$$\mathrm{PolDeg}_{\mathrm{ex}}(\text{I-J}) := \langle\|\text{I-J}\|\rangle \qquad (6)$$

$$= \sqrt{\frac{\sum_K [\rho(\text{I}) - \rho(\text{J})]^2|_K}{3 \; \sum_K [\rho(\text{I}) + \rho(\text{J})]^2|_K}}, \qquad (7)$$

where K is the observant (detection) polarization base. Exemplary results of $\langle\|$I-J$\|\rangle$ are shown in the lower panels of Fig. 5 together with the individual polarization degrees PolDeg(I-J)$|_K$. It can be observed that $\langle\|$I-J$\|\rangle$ effectively constitutes the vector norm of the polarized response of the QD via the excitation resonance. In other words, it renders the calibration of specific excitation resonances to the fundamental QD eigenstates unnecessary.

In order to determine the total spin preparation fidelity of the excitation resonances, the polarization degree can be abstracted further. This can be done irrespective of varying detection and excitation polarization bases calibration with respect to specific eigenstates and excitation resonances. The total excitation polarization degree, which is equivalent to the ground state spin preparation fidelity f_{SpinPrep}, is therefore defined as

$$f_{\mathrm{SpinPrep}} \equiv \|\mathrm{PolDeg}_{\mathrm{ex}}\| := \sqrt{\sum_{\text{I-J}} \langle\|\text{I-J}\|\rangle^2}. \qquad (8)$$

Spectra of f_{SpinPrep}, extracted from the polarization-resolved PLE spectra in analog to Fig. 5 of X_S^0, X_S^+, and $X_S^- + XX_S^0$, are summarized in Fig. 6.

By employing this method, the spin preparation fidelity of different excitation resonances can be compared effectively. For example, the polarization response of resonances $R_2^{X_S^0}$ and $R_2^{XX_S^0}$ does not show any dependence on the excitation polarization, indicating that the excited and ground states exhibit orthogonal eigenstates. Resonances $R_0^{X_S^+}$, $R_3^{X_S^+}$, $R_3^{X_S^-}$, and $R_4^{X_S^-}$ on the other hand show f_{SpinPrep} values up to 85%, demonstrating matching excited and ground spin configurations as well as spin preserving nonradiative decay processes. Heralded spin preparation of single carrier spin qubits is therefore achieved. For X_S^0 the excitation resonance induced spin memory is limited to 75%, cf. $R_0^{X_S^0}$. Due to the vacuum initial state of X_S^0, this shows that high-fidelity deterministic preparation of the X_S^0 spin state is realized using the presented quasiresonant excitation scheme. Other resonances show intermediate spin preparation fidelities, which can be attributed to either partial mismatch between excited and ground state eigenstates or nonpolarization preserving nonradiative decay
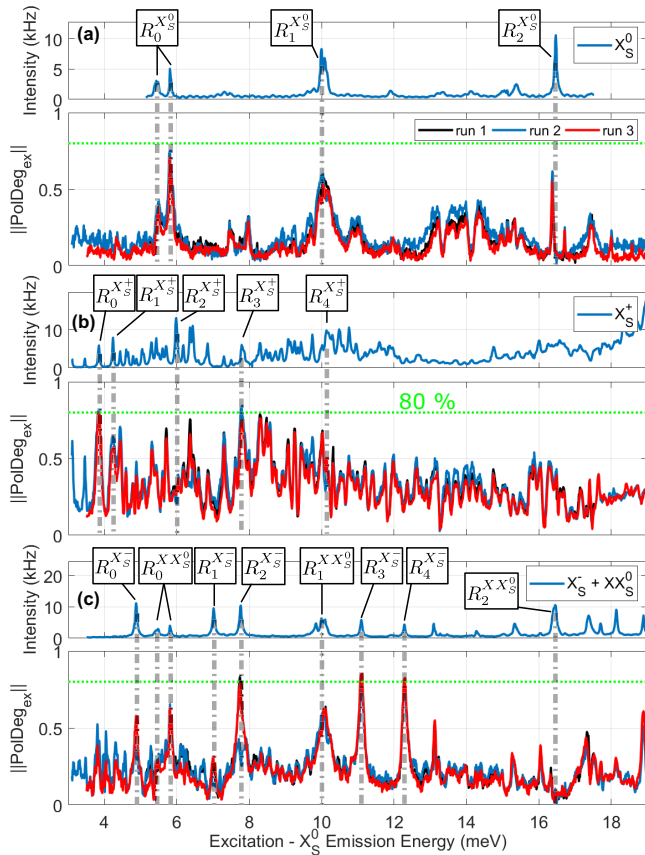
FIG. 6. Spin preparation fidelity $f_{\mathrm{SpinPrep}} \equiv \|\mathrm{PolDeg}_{\mathrm{ex}}\|$ [cf. Eq. (8)] spectra for QD s-shell transitions X_S^0, X_S^+, $X_S^- + XX_S^0$, and multiple experimental runs, more details are given in the text. Resonances of Table III are annotated by labels and gray dashed guidelines. The 80% spin preparation fidelity threshold is indicated in green.

processes. A reason for the latter would be, if more than one particle is involved in the decay process. The resonances with the highest spin preparation fidelities all belong to the s-p shell, cf. Fig. 2, indicating that resonances of this shell would be preferable for implementations of quantum spin memories based on droplet-etched GaAs QDs. It is worth noting that no external spin manipulation is performed in this study, any observed polarization change is a direct response of the QD system when subjected to polarized excitation.

Polarization-resolved PLE spectra are recorded in three separate experimental runs which feature different experimental conditions. The first, second, and third runs are optimized for detection polarization bases of X_S^0, X_S^+, and X_S^-, respectively. Additionally, weak above-band excitation (<2 nW) is employed and the excitation polarization bases are aligned using the reflection of a resonant laser in the first and third runs, while no above-band excitation and excitation calibration to $R_1^{X_S^0}$ is used in the second. The resonant excitation powers of the three runs are 1.4, 4, and 4 μW, respectively. Generally the results between different experimental runs are very consistent—underlining the validity and robustness of the method of extracting f_{SpinPrep} presented in this study. Additional verification of this method is obtained by a detailed

comparison of runs two and three around the $R_1^{X_S^+}$ resonance. This comparison is presented in the Supplemental Material [27]. Only the resonance $R_2^{X_S^-}$ shows significant deviation between the experimental runs, indicating the influence of above-band excitation for this specific excitation resonance.

III. CONCLUSIONS

Droplet-etched GaAs QDs are investigated comprehensively using polarization-resolved PL, PLE, and correlation spectroscopy. It is found that the GaAs QDs carrier dynamics depend drastically on the excitation method, e.g., in continuous wave quasiresonant excitation blinking of the X_S^0 transition is very pronounced. By modeling of the X_S^0 autocorrelation traces an eight times increase in the on-off ratio in above-band compared to quasiresonant excitation is observed. We attribute this behavior to the defect states around the QDs, similarly reported in Ref. [24]. Furthermore, the predominant charge of the QDs is shifted towards excitations with excess holes in quasiresonant excitation schemes. The lifetime of the X_S^0 transition is determined consistently using both quasiresonant and above-band correlation spectroscopy to (303 ± 6) ps. Using this information, the nonradiative decay processes of several different excitation resonances for X_S^0, X_S^+, and X_S^- transitions are investigated by pump-probe experiments. The minimal characteristic nonradiative decay times T_{NR} are estimated to 37, 88, and 29 ps, respectively, all of which can be attributed to s-p shell excitation resonances. T_{NR} is found to increase as a function of the excitation power as well as the energy of the excitation resonances. Excitation power dependent Rabi oscillations—an unambiguous sign of coherent excitation of a two-level system—are not observed for any resonance using quasiresonant pumping. This can be attributed to the finding that the parameters of the employed quasiresonant three-level scheme of the pump-probe experiments do not allow an effective reduction to a two-level system. The energetic structure of the excitation resonances is investigated using PLE spectroscopy. By employing observed properties of various excitonic complexes, specific resonances can be attributed to different energetic shells. In order to match the polarization eigenbases of the laboratory frame to the one of the QDs, the emission characteristics of its excitonic spin states both with and without external magnetic field are employed. Due to the wavelength dependent birefringency of the GaP microlens, used to enhance the collection efficiency of the QD emission [17], the polarization calibration is wavelength dependent. To effectively extract the spin preparation fidelity f_{SpinPrep} independently of the calibration of excitation and detection polarization bases an innovative method is proposed. This procedure generalizes the concept of the degree of polarization and employs measurements in 18 different excitation and detection bases and the orthogonality between bases pairs to determine f_{SpinPrep} obtained using excitation resonances. Heralded qubit spin preparation with f_{SpinPrep} of up to 85% for both X_S^+ and X_S^- as well as deterministic preparation of about 75% fidelity for X_S^0 are achieved for s-p shell type transitions.

In conclusion, the presented comprehensive investigations, methods, and findings enable the directed usage of excited state resonances to deterministically prepare basic spin states
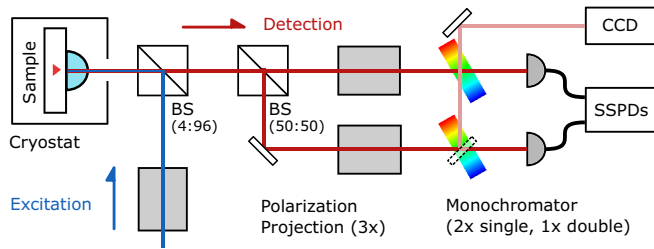
FIG. 7. Simplified schematic drawing of the experimental setup. The following abbreviations are used: Beam splitter (BS), superconducting single photon nanowire detectors (SSPDs), and charge coupled device (CCD).

in GaAs quantum dots. This fundamental ability will pave the way to use these quantum dots in a large variety of future quantum optical experiments and applications, such as QD based quantum memories [18,23,50], quantum entanglement repeaters [9,10], photon graph [6] and cluster states [7], as well as more efficient entangled photon pair sources [17,26]. Additionally, the presented study advances the understanding of droplet-etched GaAs QDs significantly. While not all aspects are explored exhaustively, it provides an ideal starting point for more detailed investigations in a variety of aspects. Examples of the latter are identification of transitions of excitonic complexes, excitation scheme dependent photonic and electronic coherences, the nature of the nonradiative decay processes, and dependency of QD properties on matrix material composition.

IV. METHODS

The presented study is performed using droplet-etched GaAs quantum dots (QDs) embedded in QD nanomembranes and attached to GaP solid immersion lenses. Samples are grown on [001] GaAs substrate using molecular beam epitaxy. The nanoholes are etched through deposition of Al droplets onto the $Al_{0.15}Ga_{0.85}As$ matrix material. Consequently, the 15 nm deep and 40 nm wide nanoholes are filled with GaAs thereby forming the QDs. The 380 nm thick $Al_{0.15}Ga_{0.85}As$ matrix material with the centrally embedded QDs is grown on top of a AlAs sacrificial layer, which is removed by selective hydrofluoric acid etching to yield the QD nanomembranes. In order to overcome the strong internal reflection of the semiconductor material due to its high refractive index ($\simeq 3.5$) and enhance the out-coupling efficiency, the QD nanomembranes are attached to GaP solid immersion lenses using a 50 nm thick layer of PMMA. This enhances the photon extraction efficiency compared to unprocessed samples by a factor of about 100. A detailed description of the growth and processing steps can be found in Refs. [17,51].

The employed experimental setup is shown as a simplified sketch in Fig. 7. The QD devices consisting of GaP

solid immersion lenses with attached QD nanomembranes are placed inside a dry closed-cycle cryostat. The cryogenic system features a z-axis 9 T superconducting magnet and a 3.8 K base temperature. Sample luminescence is collected using a aspheric lens of 0.64 NA. Photoluminescence (PL) spectroscopy is performed using a 2×0.750 m double spectrometer and gratings of either 1800 or 1200 lines/mm. The maximal spectral resolution of this system is about 15 μeV at 780 nm. The spectrometer can be configured as two independent monochromators, which is employed in auto- and cross-correlation experiments. Spectroscopic investigations are performed by a standard back-illuminated deep-depletion CCD. For PLE spectroscopy a narrow-band (100 MHz) wavelength-tuneable and wavelength-stabilized cw laser, in conjunction with the high resolution PL detection system, is employed. Wavelengths are tuned and stabilized to an absolute accuracy of 2 pm using a calibrated wavelength meter. In order to enhance the suppression of the excitation laser and separate it from the QD emission tuneable band edge filters in both excitation and detection are employed. Pump-probe experiments are performed using a wavelength tuneable and pulsed optical parametric oscillator (OPO) laser pumped by a pulsed frequency doubled fiber laser at 516 nm. The OPO laser system exhibits a repetition rate of 76.271 MHz and its pulses are shaped to a Gaussian profile of 100 GHz width (3.5 ps pulse length) using a ruled grating. For above-band excitation a HeNe laser featuring a 632.8 nm emission wavelength is employed. In order to perform polarization-resolved PL and PLE spectroscopy the polarization of the QD emission is projected onto one of the set of orthogonal polarization bases (H, V, D, A, R, L). This is achieved by using two liquid crystal variable retarders (LCVRs) and a linear polarizer. Aforementioned configuration can be calibrated to any orthogonal set of polarization bases on the Poincaré sphere and enables the compensation of the mismatch between QD and laboratory polarization eigenbases. The accuracy of LCVR calibration was determined to about 0.95 using a polarimeter. Three independent polarization projector units are employed: two in the detection arms and one in the excitation path, cf. Fig. 7. Correlation spectroscopy is performed by time-resolved correlation of electronic signals from superconducting nanowire single photon detectors (SSPDs). The single- (two-) photon timing resolution δ_{1det} (δ_{2det}) of this system is about 53 (75) ps.

[1] J. I. Cirac, P. Zoller, H. J. Kimble, and H. Mabuchi, Quantum State Transfer and Entanglement Distribution Among Distant Nodes in a Quantum Network, Phys. Rev. Lett. **78**, 3221 (1997).

[2] H. J. Kimble, The quantum internet, Nature (London) **453**, 1023 (2008).

[3] C. Simon, Towards a global quantum network, Nat. Photonics **11**, 678 (2017).

[4] P. van Loock, W. Alt, C. Becher, O. Benson, H. Boche, C. Deppe, J. Eschner, S. Höfling, D. Meschede, P. Michler, F. Schmidt, and H. Weinfurter, Extending quantum links: Modules for fiber- and memory-based quantum repeaters, Adv. Quantum Technol. **3**, 1900141 (2020).

[5] S. Ritter, C. Nölleke, C. Hahn, A. Reiserer, A. Neuzner, M. Uphoff, M. Mücke, E. Figueroa, J. Bochmann, and G. Rempe, An elementary quantum network of single atoms in optical cavities, Nature (London) **484**, 195 (2012).

[6] X.-L. Wang, L.-K. Chen, W. Li, H.-L. Huang, C. Liu, C. Chen, Y.-H. Luo, Z.-E. Su, D. Wu, Z.-D. Li, H. Lu, Y. Hu, X. Jiang, C.-Z. Peng, L. Li, N.-L. Liu, Y.-A. Chen, C.-Y. Lu, and J.-W. Pan, Experimental Ten-Photon Entanglement, Phys. Rev. Lett. **117**, 210502 (2016).

[7] I. Schwartz, D. Cogan, E. R. Schmidgall, Y. Don, L. Gantz, O. Kenneth, N. H. Lindner, and D. Gershoni, Deterministic generation of a cluster state of entangled photons, Science **354**, 434 (2016).

[8] S.-K. Liao, W.-Q. Cai, J. Handsteiner, B. Liu, J. Yin, L. Zhang, D. Rauch, M. Fink, J.-G. Ren, W.-Y. Liu, Y. Li, Q. Shen, Y. Cao, F.-Z. Li, J.-F. Wang, Y.-M. Huang, L. Deng, T. Xi, L. Ma, T. Hu *et al.*, Satellite-Relayed Intercontinental Quantum Network, Phys. Rev. Lett. **120**, 030501 (2018).

[9] M. Zopf, R. Keil, Y. Chen, J. Yang, D. Chen, F. Ding, and O. G. Schmidt, Entanglement Swapping with Semiconductor-Generated Photons Violates Bell's Inequality, Phys. Rev. Lett. **123**, 160502 (2019).

[10] F. Basso Basset, M. B. Rota, C. Schimpf, D. Tedeschi, K. D. Zeuner, S. F. Covre da Silva, M. Reindl, V. Zwiller, K. D. Jöns, A. Rastelli, and R. Trotta, Entanglement Swapping with Photons Generated on Demand by a Quantum Dot, Phys. Rev. Lett. **123**, 160501 (2019).

[11] M. K. Bhaskar, R. Riedinger, B. Machielse, D. S. Levonian, C. T. Nguyen, E. N. Knall, H. Park, D. Englund, M. Lončar, D. D. Sukachev, and M. D. Lukin, Experimental demonstration of memory-enhanced quantum communication, Nature (London) **580**, 60 (2020).

[12] M. Körber, O. Morin, S. Langenfeld, A. Neuzner, S. Ritter, and G. Rempe, Decoherence-protected memory for a single-photon qubit, Nat. Photonics **12**, 18 (2018).

[13] M. H. Abobeih, J. Cramer, M. A. Bakker, N. Kalb, M. Markham, D. J. Twitchen, and T. H. Taminiau, One-second coherence for a single electron spin coupled to a multi-qubit nuclear-spin environment, Nat. Commun. **9**, 1 (2018).

[14] J. R. Schaibley, A. P. Burgers, G. A. McCracken, L.-M. Duan, P. R. Berman, D. G. Steel, A. S. Bracker, D. Gammon, and L. J. Sham, Demonstration of Quantum Entanglement between a Single Electron Spin Confined to an InAs Quantum Dot and a Photon, Phys. Rev. Lett. **110**, 167401 (2013).

[15] W. Gao, P. Fallahi, E. Togan, J. Miguel-Sánchez, and A. Imamoğlu, Observation of entanglement between a quantum dot spin and a single photon, Nature (London) **491**, 426 (2012).

[16] I. Schwartz, E. R. Schmidgall, L. Gantz, D. Cogan, E. Bordo, Y. Don, M. Zielinski, and D. Gershoni, Deterministic Writing and Control of the Dark Exciton Spin Using Single Short Optical Pulses, Phys. Rev. X **5**, 011009 (2015).

[17] Y. Chen, M. Zopf, R. Keil, F. Ding, and O. G. Schmidt, Highly-efficient extraction of entangled photons from quantum dots using a broadband optical antenna, Nat. Commun. **9**, 2994 (2018).

[18] D. Cogan, O. Kenneth, N. H. Lindner, G. Peniakov, C. Hopfmann, D. Dalacu, P. J. Poole, P. Hawrylak, and D. Gershoni, Depolarization of Electronic Spin Qubits Confined in Semiconductor Quantum Dots, Phys. Rev. X **8**, 041050 (2018).

[19] N. Bloembergen, E. M. Purcell, and R. V. Pound, Relaxation effects in nuclear magnetic resonance absorption, Phys. Rev. **73**, 679 (1948).

[20] D. Gammon, A. L. Efros, T. A. Kennedy, M. Rosen, D. S. Katzer, D. Park, S. W. Brown, V. L. Korenev, and I. A. Merkulov, Electron and Nuclear Spin Interactions in the Optical Spectra of Single GaAs Quantum Dots, Phys. Rev. Lett. **86**, 5176 (2001).

[21] A. Greilich, D. R. Yakovlev, A. Shabaev, A. L. Efros, I. A. Yugova, R. Oulton, V. Stavarache, D. Reuter, A. Wieck, and M. Bayer, Mode locking of electron spin coherences in singly charged quantum dots, Science **313**, 341 (2006).

[22] A. Högele, M. Kroner, C. Latta, M. Claassen, I. Carusotto, C. Bulutay, and A. Imamoglu, Dynamic Nuclear Spin Polarization in the Resonant Laser Excitation of an InGaAs Quantum Dot, Phys. Rev. Lett. **108**, 197403 (2012).

[23] R. Stockill, C. Le Gall, C. Matthiesen, L. Huthmacher, E. Clarke, M. Hugues, and M. Atatüre, Quantum dot spin coherence governed by a strained nuclear environment, Nat. Commun. **7**, 12745 (2016).

[24] J.-P. Jahn, M. Munsch, L. Béguin, A. V. Kuhlmann, M. Renggli, Y. Huo, F. Ding, R. Trotta, M. Reindl, O. G. Schmidt, A. Rastelli, P. Treutlein, and R. J. Warburton, An artificial Rb atom in a semiconductor with lifetime-limited linewidth, Phys. Rev. B **92**, 245439 (2015).

[25] R. Keil, M. Zopf, Y. Chen, B. Höfer, J. Zhang, F. Ding, and O. G. Schmidt, Solid-state ensemble of highly entangled photon sources at rubidium atomic transitions, Nat. Commun. **8**, 15501 (2017).

[26] C. Hopfmann, W. Nie, N. L. Sharma, C. Weigelt, F. Ding, and O. G. Schmidt, Maximally entangled and gigahertz-clocked on-demand photon pair source, Phys. Rev. B **103**, 075413 (2021).

[27] See Supplemental Material at http://link.aps.org/supplemental/10.1103/PhysRevB.104.075301 for more information on exciton fine structure, excitation schemes, correlation spectroscopy. polarization states, magnetic field dependence, and excitation spectroscopy linewidths.

[28] T. H. Stievater, X. Li, D. G. Steel, D. Gammon, D. S. Katzer, D. Park, C. Piermarocchi, and L. J. Sham, Rabi Oscillations of Excitons in Single Quantum Dots, Phys. Rev. Lett. **87**, 133603 (2001).

[29] H. Kamada, H. Gotoh, J. Temmyo, T. Takagahara, and H. Ando, Exciton Rabi Oscillation in a Single Quantum Dot, Phys. Rev. Lett. **87**, 246401 (2001).

[30] S. Stufler, P. Machnikowski, P. Ester, M. Bichler, V. M. Axt, T. Kuhn, and A. Zrenner, Two-photon Rabi oscillations in a single $In_xGa_{1-x}As - GaAs$ quantum dot, Phys. Rev. B **73**, 125304 (2006).

[31] A. Fox, M. Fox, and D. Fox, *Quantum Optics: An Introduction*, Oxford Master Series in Physics (Oxford University Press, Oxford, 2006).

[32] Y. Benny, S. Khatsevich, Y. Kodriano, E. Poem, R. Presman, D. Galushko, P. M. Petroff, and D. Gershoni, Coherent Optical Writing and Reading of the Exciton Spin State in Single Quantum Dots, Phys. Rev. Lett. **106**, 040504 (2011).

[33] K. De Greve, L. Yu, P. L. McMahon, J. S. Pelc, C. M. Natarajan, N. Y. Kim, E. Abe, S. Maier, C. Schneider, M. Kamp, S. Höfling, R. H. Hadfield, A. Forchel, M. M. Fejer, and Y. Yamamoto, Quantum-dot spin-photon entanglement via frequency downconversion to telecom wavelength, Nature (London) **491**, 421 (2012).

[34] D. Huber, M. Reindl, Y. Huo, H. Huang, J. S. Wildmann, O. G. Schmidt, A. Rastelli, and R. Trotta, Highly indistinguishable and strongly entangled photons from symmetric GaAs quantum dots, Nat. Commun. **8**, 15506 (2017).

[35] P. Michler, Ed., *Single Quantum Dots*, Topics in Applied Physics No. 90 (Springer, New York, 2003).

[36] Y. Benny, Y. Kodriano, E. Poem, S. Khatsevitch, D. Gershoni, and P. M. Petroff, Two-photon photoluminescence excitation spectroscopy of single quantum dots, Phys. Rev. B **84**, 075473 (2011).

[37] D. A. B. Miller, D. S. Chemla, T. C. Damen, A. C. Gossard, W. Wiegmann, T. H. Wood, and C. A. Burrus, Band-Edge Electroabsorption in Quantum Well Structures: The Quantum-Confined Stark Effect, Phys. Rev. Lett. **53**, 2173 (1984).

[38] J. Seufert, R. Weigand, G. Bacher, T. Kümmell, A. Forchel, K. Leonardi, and D. Hommel, Spectral diffusion of the exciton transition in a single self-organized quantum dot, Appl. Phys. Lett. **76**, 1872 (2000).

[39] M. Abbarchi, F. Troiani, C. Mastrandrea, G. Goldoni, T. Kuroda, T. Mano, K. Sakoda, N. Koguchi, S. Sanguinetti, A. Vinattieri, and M. Gurioli, Spectral diffusion and line broadening in single self-assembled GaAs-AlGaAs quantum dot photoluminescence, Appl. Phys. Lett. **93**, 162101 (2008).

[40] L. Besombes, J. J. Baumberg, and J. Motohisa, Coherent Spectroscopy of Optically Gated Charged Single InGaAs Quantum Dots, Phys. Rev. Lett. **90**, 257402 (2003).

[41] Y. Benny, Y. Kodriano, E. Poem, D. Gershoni, T. A. Truong, and P. M. Petroff, Excitation spectroscopy of single quantum dots at tunable positive, neutral, and negative charge states, Phys. Rev. B **86**, 085306 (2012).

[42] C. Santori, D. Fattal, M. Pelton, G. S. Solomon, and Y. Yamamoto, Polarization-correlated photon pairs from a single quantum dot, Phys. Rev. B **66**, 045308 (2002).

[43] M. Bayer, G. Ortner, O. Stern, A. Kuther, A. A. Gorbunov, A. Forchel, P. Hawrylak, S. Fafard, K. Hinzer, T. L. Reinecke, S. N. Walck, J. P. Reithmaier, F. Klopf, and F. Schäfer, Fine structure of neutral and charged excitons in self-assembled In(Ga)As/(Al)GaAs quantum dots, Phys. Rev. B **65**, 195315 (2002).

[44] E. Siebert, T. Warming, A. Schliwa, E. Stock, M. Winkelnkemper, S. Rodt, and D. Bimberg, Spectroscopic access to single-hole energies in InAs/GaAs quantum dots, Phys. Rev. B **79**, 205321 (2009).

[45] T. Warming, E. Siebert, A. Schliwa, E. Stock, R. Zimmermann, and D. Bimberg, Hole-hole and electron-hole exchange interactions in single InAs/GaAs quantum dots, Phys. Rev. B **79**, 125316 (2009).

[46] N. Bohr, *Rydberg's Discovery of the Spectral Laws* (C.W.K. Gleerup, Lund, Sweden, 1954).

[47] Y. Benny, R. Presman, Y. Kodriano, E. Poem, D. Gershoni, T. A. Truong, and P. M. Petroff, Electron-hole spin flip-flop in semiconductor quantum dots, Phys. Rev. B **89**, 035316 (2014).

[48] S. Adachi, *Properties of Aluminium Gallium Arsenide*, 7 (IET, Stevenage, UK, 1993).

[49] H. A. Kramers, Théorie générale de la rotation paramagnétique dans les cristaux, Proc. Acad. Sci. Amsterdam **33**, 959 (1930).

[50] E. A. Chekhovich, S. F. C. da Silva, and A. Rastelli, Nuclear spin quantum register in an optically active semiconductor quantum dot, Nat. Nanotechnol. **15**, 999 (2020).

[51] Z. M. Wang, B. Liang, K. Sablon, and G. Salamo, Nanoholes fabricated by self-assembled gallium nanodrill on GaAs (100), Appl. Phys. Lett. **90**, 113120 (2007).